Theoretical and numerical analysis of the corneal air puff test

Irene Simonini [a], Maurizio Angelillo [b], Anna Pandolfi [c,*]

[a] Mathematics Department, Politecnico di Milano, 20133 Milano, Italy
[b] Civil Engineering Department, University of Salerno, 84084 Fisciano, Italy
[c] DICA, Politecnico di Milano, 20133 Milano, Italy

A B S T R A C T

Ocular analyzers are used in the current clinical practice to estimate, by means of a rapid air jet, the intraocular pressure and other eye's parameters. In this study, we model the biomechanical response of the human cornea to the dynamic test with two approaches. In the first approach, the corneal system undergoing the air puff test is regarded as a harmonic oscillator. In the second approach, we use patient-specific geometries and the finite element method to simulate the dynamic test on surgically treated corneas. In spite of the different levels of approximation, the qualitative response of the two models is very similar, and the most meaningful results of both models are not significantly affected by the inclusion of viscosity of the corneal material in the dynamic analysis. Finite element calculations reproduce the observed snap-through of the corneal shell, including two applanate configurations, and compare well with in vivo images provided by ocular analyzers, suggesting that the mechanical response of the cornea to the air puff test is actually driven only by the elasticity of the stromal tissue. These observations agree with the dynamic characteristics of the test, since the frequency of the air puff impulse is several orders of magnitude larger than the reciprocal of any reasonable relaxation time for the material, downplaying the role of viscosity during the fast snap-through phase.

1. Introduction

The cornea, the external convex–concave spherical lens of the eye, has the main functions to deviate the light rays onto the retina and to protect the delicate interior components of the eye. The spherical shape of the cornea is maintained by the action of the intraocular pressure (IOP), whose physiological range is 12–20 mmHg.

High IOP values are in general associated to pathological situations, such as glaucoma (Farandos et al., 2015). Early detection and monitoring of glaucoma require frequent IOP measurements through a specific device called tonometer. The tonometer applies a pressure on a delimited area of the external surface of the cornea, and IOP measurements are taken when a particular configuration is reached. Most tonometers commonly used in the clinical practice are based on static contact between instrument and cornea. Among static tonometers, the so-called Goldmann tonometer (GT) is considered to be the standard. When the tonometer's head, in contact with the cornea, detects the applanation of the portion of the corneal surface, it returns an estimate of the IOP (Goldmann and Schmidt, 1957). Like all non-invasive methods, the GT is inherently imprecise. Moreover, its measurements are based on the assumption that the effects of the corneal rigidity and the effects due to the presence of the tear film cancel out. But this is not always the case, especially if the cornea has been

* Corresponding author.
E-mail addresses: irene.simonini@polimi.it (I. Simonini), mangelil@unisa.it (M. Angelillo), anna.pandolfi@polimi.it (A. Pandolfi).

reprofiled by laser ablation refractive surgery (Chihara, 2008).

Drawbacks of static tonometry have been outwitted by the recent development of dynamic tonometers based on high speed camera imaging, such as the Ocular Response Analyzer (ORA; Reichert, Inc., Buffalo, NY), and the CorVis ST (CorVis ST; Oculus Optikgerate GmbH, Wetzlar, Germany). These advanced optical instruments use a rapid single air jet to modify visibly and temporarily the corneal shape. During the air puff test, the cornea snaps from its original convex shape to a locally concave shape, passing through two configurations characterized by an applanate zone. Applanation times and other shapes of the cornea during the test are used to compute a number of different parameters, expected to have some relevance in the biomechanical behavior of the cornea. Regrettably, none of them is clearly understood, because they cannot be related directly to the material properties of the cornea, nor to the eye's IOP (Martinez de la Casa et al., 2006; Piñero and Alcón, 2014). Some of the parameters supplied by the ORA have gained a certain level of popularity, in particular the corneal hysteresis (CH), defined as the difference between the pressures of a symmetric internal supply air plenum curve at the times of the two applanations (Luce, 2005). In general, the value of the second applanation pressure is smaller than the first applanation pressure, and the pressure drop roughly correlates to a sort of corneal “strength”. According to the manufacturer, CH is an assessment of the cornea's ability to absorb and dissipate energy. This theory has been supported by some authors, which interpreted CH as an indicator of viscous and elastic properties of the cornea (Glass et al., 2008).

The dynamic features of the air puff test have been analyzed in recent studies. A numerical interpretation of the air puff test in dynamic terms, based on a simple one degree-of-freedom model, has been proposed in Han et al. (2014). Finite element models of the test, that account for the fluid-dynamics of the air jet, have been presented in axis-symmetric setting (Kling et al., 2014), using a pressure space–time profile obtained by combining preliminary CFD calculations and air jet pressure measurements taken during the test; and in fully tridimensional setting (Ariza-Gracia et al., 2015; Sinha Roy et al., 2015), using a CFD approach to account for the fluid–solid interaction between the air jet and the anterior surface of the cornea. Along this line, the main goal of this study is to understand whether the behavior of the cornea during the air puff test is driven by elasticity or there is an important contribution of material viscosity. Additionally, we want to understand how geometrical changes due to corneal laser refractive surgery may affect the results of the test.

We analyze the behavior of the corneal system undergoing the air puff test by using two different approaches, which differ in terms of conceptual complexity and amount of delivered results. In the first simplified approach, we approximate the corneal shell as a one-degree-of-freedom (1DOF) dynamic system, with the aim of understanding the fundamental physics underlying the air puff test. The simplicity of the model, characterized by a mass, a spring, and a dashpot, leads to an analytical solution that allows to identify the main aspects of the process and the relevance of the parameters governing the air puff test. In particular, the displacement and velocity of the mass are obtained in closed-form, and the results are useful to distinguish the effects of viscosity and elasticity, as conceived in mechanics of materials. The second approach is based on a fully tridimensional geometrically patient-specific finite element model of the human cornea (PSFE), reconstructed from digital data acquired on healthy patients through a corneal topographer (Sirius CSO, Scandicci, Italy). The PSFE model allows us to simulate accurately the response of the cornea to the air puff tests. In the limits of the current technology, the PSFE model has been proved to be reliable and predictive in quasi-static simulations (Sánchez et al., 2014; Simonini and Pandolfi, 2015). Our results agree with the experimental data provided by clinical ocular instruments.

The two models, albeit far apart in accuracy and apparently weakly correlated, compare reasonably well in terms of qualitative response, and agree in revealing the dominant aspects of the mechanics of the air puff test. The reason that moved us to analyze the simplified 1DOF model is the intuition that the mechanical response of the cornea's material to the air puff test is primarily—at least in the loading phase, i.e., when the air pressure is applied—an undamped dynamic phenomenon, where time scales are not long enough to activate time-dependent effects in the cornea's materials. The significance of the 1DOF model and its correlation to the sophisticated PSFE model can be grasped by comparing the first natural frequency of cornea and filling fluid system with the frequency of the air puff jet. As it will be shown later, the closeness of the two frequencies suggests that the process is dominated by dynamics, thus inertia effects prevail over other time dependent aspects. We can verify this intuitive idea using a 1DOF system, and assess qualitatively the influence of inertia and damping.

The paper is organized as follows. In Section 2.1 we describe the output of two ocular instruments used to perform the air puff test on human corneas. In Section 2.2 we describe the 1DOF model and in Section 2.3 the PSFE model, both used to simulate the air puff test. Results of the numerical investigations are collected in Section 3. In Section 4 we compare numerical and experimental results (taken from the literature) on air puff tests and discuss the possibility to use the test for the characterization of the corneal material properties.

2. The air puff test and the numerical models

2.1. Clinical ocular instruments for air puff tests

We refer to air puff tests carried out with two common clinical optical instruments. The sudden pulse exerted by these instruments causes the inwards motion of the cornea, which passes through an applanation, and successively snaps into a slight concavity. When the air pulse pressure decreases, the elastic corneal tissue recovers the original configuration, passing through a second applanation. Some instrument provides the time history of the jet air pressure and of a light signal intensity reflected by the corneal anterior surface, from where it is possible to derive information on the deformative state of the cornea.

The ORA system utilizes a precisely metered collimated air pulse to deflect dynamically the cornea. An advanced electro-optical collimation system, automatically aligned to the patient's eye, monitors the cornea deflection, recording in 400 images the intensity of the light signals. Light signals reach peak values at the applanation times and the two corresponding pressures, associated to the air jet, are recorded. The duration of the pulse is 20 ms, and the duration of the whole recorded process is about 30 ms (Luce, 2005). ORA does not read the corneal deflection, but provides the pressure history during the test: the device applies a pressure calibrated to the patient, adjusting the air impulse after detecting the first applanation (Ambrósio et al., 2011). This accommodation renders the pressure and the measurement not repeatable even on the same cornea (Roberts, 2014).

The CorVis ST system is a more recent noncontact tonometer with an operation system similar to ORA, able to operate on 1–60 mmHg range of IOP (Hong et al., 2013). CorVis ST uses a high-speed Scheimpflug-camera (4330 frames/s) to record the motion of the cornea during the air puff test. Images are taken along the nasal–temporal (NT) meridian, and visualize the changing shape of both anterior and posterior profiles of the cornea. The resulting images (about 140) are later displayed on the built-in control panel in ultra-slow-motion (Hon and Lam, 2013), see Fig. 1 (courtesy of Oculus Optikgerate GmbH). CorVis ST does not record the pressure profile, whose maximum value is not specified, although it applies a constant impulse over an assigned time interval (1/157 s).

In the following, we model a test corresponding to the one performed by CorVis ST. Although the actual space and the time profile of the air jet pressure and its maximum value are not provided by the instrument, the imprint of the air jet on the anterior corneal surface can be estimated, through preliminary parametric analyses, using analytical expressions, as explained in Section 2.3.

2.2. Harmonic oscillator model (1DOF)

We utilize a one-dimensional dynamic oscillator (1DOF) to model the behavior of the cornea under the action of a brief air pulse, Fig. 2(a), see also Han et al. (2014). The simplicity of the model should not be considered detrimental to its conceptual validity. Simple dynamic models are useful to clarify the significance of the physical parameters of a test, since they give the possibility to work with analytical solutions. We remember that the recurse to one degree-of-freedom analogs is very common in practical design of complex mechanical and electrical systems, and is of great utility in the conceptual phase of designing innovative materials, characterized by an internal structure. We begin by considering a purely elastic system, see Fig. 2(b). The cornea elasticity is represented by the stiffness k of a spring, and its inertia by a point mass m. The IOP pressure is represented by a constant point load $P > 0$. The system is excited by a single half wave sinusoidal load $p(t)$ of angular frequency ω, period T, and amplitude $p_0 > 0$

$$p(t) = p_0\, h(t) \sin \omega t, \quad \omega = \frac{2\pi}{T}, \tag{1}$$

modeling in the simplest way the air jet pressure; $h(t)$ is taken to be 1 in the interval $0 \le t \le T/2$ and 0 otherwise, to restrict the air jet pressure over half a period. We denote by x the displacement of the mass and write the equation of motion as

$$m\ddot{x} + kx = P - p_0\, h(t) \sin \omega t, \tag{2}$$

where $\ddot{x}$ is the mass acceleration. The initial conditions are

$$x(0) = x_0 = \frac{P}{k}, \quad \dot{x}(0) = 0, \tag{3}$$

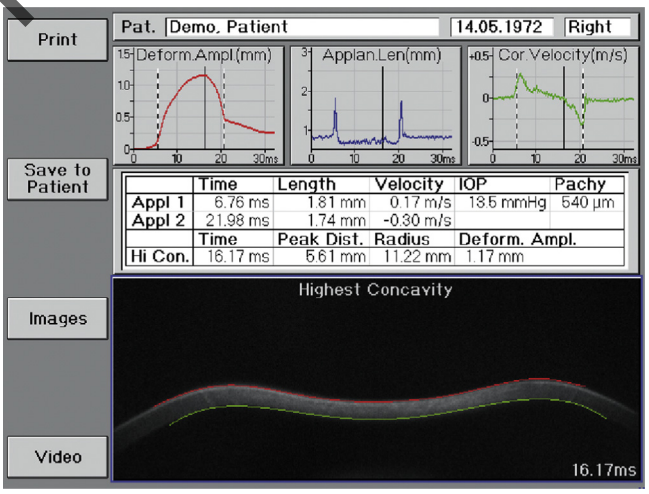

Fig. 1. Ocular analyzer's output. Example of CorVis ST output (courtesy of Oculus Optikgerate GmbH).

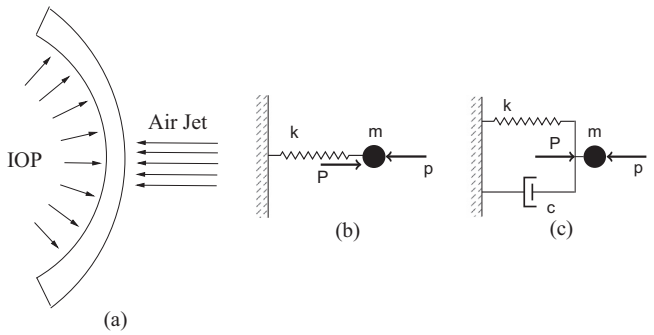

Fig. 2. Simple 1DOF model. (a) Schematic of the air puff test and corresponding one-degree-of-freedom rheologic models. (b) Elastic oscillator. (c) Viscoelastic oscillator in the Kelvin–Voigt configuration.

where x_0 denotes the static equilibrium position. By introducing the natural frequency of the system Ω

$$\Omega = \sqrt{\frac{k}{m}} \tag{4}$$

the variables t and x can be reduced to a dimensionless form as

$$\tau = \Omega t, \quad y(\tau) = \frac{x(t)}{x_0} = \frac{m\Omega^2}{P}\, x(t), \tag{5}$$

and Eq. (2) can be rendered as

$$y'' + y = 1 - \alpha\, h(\tau) \sin \beta\tau, \quad \alpha = \frac{p_0}{P}, \quad \beta = \frac{\omega}{\Omega}, \tag{6}$$

where $h(\tau)$ is 1 in $0 \le \tau \le \pi/\beta$ and 0 otherwise, and y'' denotes the second derivative with respect to τ. The constant $\alpha > 1$ measures the relative intensity of the dynamic load (jet pressure) with respect to the static load (IOP), and the constant β measures the ratio between the excitation frequency and the natural frequency. The initial conditions (3) become

$$y(0) = 1, \quad y'(0) = 0. \tag{7}$$

The closed form solution of the problem is well known and reads

$$y(\tau) = -1 + \frac{\alpha}{\beta^2 - 1}(\beta \sin \tau - \sin \beta\tau). \tag{8}$$

Note that the case $\beta = 1$ implies resonance, and unbounded solution. To account for time dependency, the simple oscillator is integrated with a dashpot in the configuration of the Kelvin–Voigt model, characterized by a viscous damping coefficient $c > 0$, see Fig. 2(c). The dashpot reacts with a viscous force proportional to the mass velocity $\dot{x}$ and the equation of motion (2) becomes

$$m\ddot{x} + c\dot{x} + kx = P - p_0 h(t) \sin \omega t, \tag{9}$$

and in dimensionless form

$$y'' + 2\xi y' + y = -1 + \alpha \sin \beta\tau, \quad \xi = \frac{c}{2\sqrt{mk}} \tag{10}$$

where ξ is the damping ratio. The solution of the differential equation (10) is a complex exponential. The analytical solution of the two differential equations (6) and (10) for different values of the parameters has been obtained with the software Maple 17 (Maplesoft, Waterloo Maple Inc, Ontario, Canada). We note that our analysis differs from the one described in Han et al. (2014) in terms of boundary conditions and of solution approach. Our boundary conditions include the assignment of the initial velocity of the mass, assumed to be null, and not the final position of the mass (see Eq. (3) in Han et al., 2014). Moreover, we resort to solve the equation of motion analytically, while in Han et al. (2014) the solution was achieved numerically by using finite differences.

2.3. Finite element model

The simple 1DOF model uses global elasticity and viscosity parameters that cannot be directly used in the material modeling of the corneal tissue. In view of exploiting the air jet test for the characterization of corneal material properties, it is necessary to use a more sophisticated numerical model, based on the description of the cornea as a continuum. The finite element method has been widely used for modeling the behavior of the cornea, mainly considering static conditions, see,

e.g., Bryant and McDonnell (1996), Cabrera Fernández et al. (2005), Pinsky et al. (2005), Alastrué et al. (2006), Elsheikh (2010), and Sinha Roy and Dupps (2011).

To model the biomechanics of cornea, in the last decade we have been developing a in-house finite element code that has been used in several quasi-static studies (Pandolfi and Manganiello, 2006; Pandolfi and Holzapfel, 2008; Pandolfi et al., 2009; Sánchez et al., 2014; Simonini and Pandolfi, 2015). Distinguished features of current version of our finite element code are (i) the possibility to include patient-specific geometries; (ii) a stochastic fiber distributed material model, to describe the complex architecture of reinforcing collagen fibrils in the stromal tissue; (iii) the automatic identification of the stress-free configuration of the cornea; (iv) the customization of the material parameters.

A known and controlled limitation of our model is that we consider only the main corneal layer (stroma) and disregard the thin anterior and posterior membranes, that have negligible effects on the mechanical stiffness of the cornea. A second limitation is that the model does not include the adjacent parts of the eye, i.e., the white sclera and the iris, which are accounted for only in terms of compliant boundaries at the limbus (Sánchez et al., 2014). The missing eye components are not included in the model for the lack of knowledge of their in vivo mechanical properties. The inclusion in the model of limbus, iris, and sclera, characterized by hypothetical material parameters, will pollute the numerical analysis with more uncertainties than the exclusion of such parts would do. Additionally, the images obtained from ocular analyzers do not include limbus and sclera, ruling out the possibility of using *ad hoc* identification procedures. As explained in Pandolfi and Holzapfel (2008), a reasonable choice of the cornea's boundary condition may narrow the effects of these deficiencies.

Implications of using corneal buttons instead of whole eyeballs in air puff tests on pig corneas have been examined in a recent experimental study (Kling and Marcos, 2013); small differences in the apical displacement history have emerged. Moreover, such differences are characterized by a rather large dispersion and, because of the elliptical shape of pig corneas, results obtained for pig eyes cannot be easily extended to human eyes.

We generate patient-specific finite element models of the human cornea using an *ad hoc* software. A solid model generator, specifically developed to create human cornea models from a few geometrical parameters of standard clinical measurements, was first presented in Pandolfi and Manganiello (2006). Customized models based on corneal topographies of patients undergoing laser corneal refractive surgery were used to predict the outcomes of photorefractive keratectomy (Sánchez et al., 2014). Patient-specific geometries, constructed from sets of anterior corneal surface coordinates and thicknesses supplied by ocular topographers, were illustrated in Simonini and Pandolfi (2015). Patient-specific models were used to analyze the stress distribution and the variation of the cornea's refractive parameters with the IOP. Independently of its origin, the cornea solid model is automatically discretized, at the desired level of refinement, in standard finite elements, e.g., 8-node bricks with linear interpolation of the displacements, see Fig. 3.

The knowledge of the sole patient-specific geometry of the cornea is not sufficient to produce an accurate numerical model. A key point is that the topographer images refer to the cornea in its physiological configuration, reacting to the IOP. A stress analysis requires the determination of the unknown stress-free configuration, corresponding to a null IOP. An automatic procedure that allows for the recovery of the stress-free configuration was proposed in Pandolfi and Manganiello (2006), improved in Sánchez et al. (2014), and optimized in Simonini and Pandolfi (2015). The procedure is briefly recalled

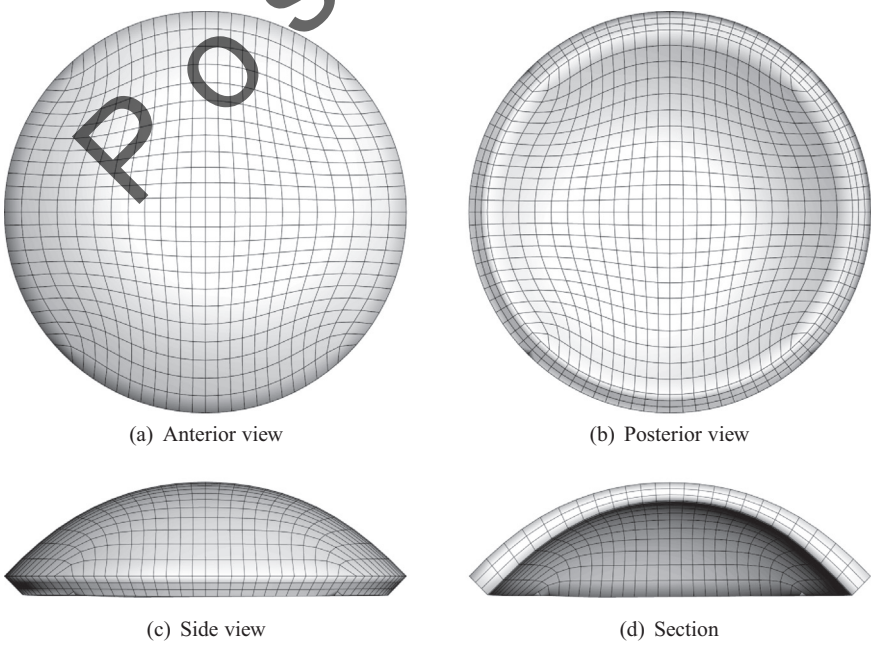

(a) Anterior view (b) Posterior view

(c) Side view (d) Section

Fig. 3. PSFE model of the cornea. Finite element mesh comprising 2500 nodes and 1728 8-node elements. The geometry refers to the stress-free configuration of the reference patient.

in Appendix A.

In the present study we confine our attention to the information on the material model that can be retrieved from the air puff test. We use an elastic anisotropic material model, whose parameters have been identified by means of quasi-static analyses in previous studies (Sánchez et al., 2014; Simonini and Pandolfi, 2015), and aim at understanding how relevant the viscosity of the corneal material can be on the outcomes of the air puff test.

The material model adopted for the cornea is hyperelastic and fiber-reinforced (Pandolfi and Vasta, 2012), with a statistical von Mises type distribution of the fibril orientation that accounts only for fibrils in extension. In the evaluation of the stresses, this model has been proven not to produce large errors, typical, indeed, of generalized structure tensor models (Gasser et al., 2006). The material is assumed to be quasi-incompressible, and the behavior of the proteoglycan matrix of the stroma and the reinforcing collagen fibrils are modeled separately. Thus, the strain energy density function Ψ is assumed to be the sum of three independent contributions with full separation of the arguments:

$$\Psi = \Psi_{\text{vol}}(J) + \Psi_{\text{iso}}(\bar{I}_1, \bar{I}_2) + \Psi_{\text{aniso}}(\overline{I}^{*}_{4M}). \tag{11}$$

The contribution Ψ_{vol} accounts for the volumetric elastic response and depends on the Jacobian $J = \det \mathbf{F}$, where $\mathbf{F} = \partial\mathbf{x}/\partial\mathbf{X}$ is the deformation gradient. The strain energy Ψ_{vol}, to be considered as a penalty term to enforce the incompressibility constraint, has the operative form

$$\Psi_{\text{vol}}(J) = \frac{1}{4} K (J^2 - 1 - 2 \log J), \tag{12}$$

where K is a stiffness coefficient related to the bulk modulus. The contribution Ψ_{iso} describes the behavior of the isotropic components of the material, and depends on the first and second invariants, $\bar{I}_1$ and $\bar{I}_2$ (see Appendix B) of the isochoric Cauchy–Green deformation tensor $\overline{\mathbf{C}} = \overline{\mathbf{F}}^T\overline{\mathbf{F}}$, with $\overline{\mathbf{F}} = J^{-1/3}\mathbf{F}$, according to Mooney–Rivlin's model

$$\Psi_{\text{iso}}(\bar{I}_1, \bar{I}_2) = \tfrac{1}{2}\mu_1(\bar{I}_1 - 3) + \tfrac{1}{2}\mu_2(\bar{I}_2 - 3), \tag{13}$$

where $\mu = \mu_1 + \mu_2$ is the shear modulus of the material. The contribution Ψ_{aniso} addresses the anisotropic contribution of two non-randomly oriented families of collagen fibrils. The M fibril family is defined in terms of a unit vector field, $\mathbf{a}_M(\mathbf{x})$, that identifies the dominant orientation of the fibrils belonging to the family M, and by a dispersion coefficient $b(\mathbf{x})$, cf. Sánchez et al. (2014). The anisotropic strain energy function Ψ_{aniso} used in the model is

$$\Psi_{\text{aniso}}(\overline{I}^{*}_{4M}, K^{*}_{M}) = \sum_{M=1}^{2} \frac{k_1}{2k_2} \exp\left[k_2\left(\overline{I}^{*}_{4M} - 1\right)^2\right](1 + K^{*}_{M}\sigma^2_{\overline{I}^{*}_{4M}}), \tag{14}$$

where k_1 is a stiffness parameter for fibrils in moderate extension, and k_2 is a dimensionless rigidity parameter that describes the behavior of fibrils in large extension. The expression of the variables $\overline{I}^{*}_{4M}$ and K^{*}_{M} in (14) is reported in Appendix B. The material model is characterized by five parameters: the bulk modulus K, two shear moduli μ_1 and μ_2 for the Mooney–Rivlin model, the fibril stiffness k_1, and the fibril rigidity k_2.

The architecture of the fibrils is in line with the most recent findings of X-ray imaging on ex vivo corneas (Meek and Boote, 2009), with different levels of the dispersion $b(\mathbf{x})$ in different locations of the cornea. Fibrils are strongly aligned at the center, where they follow an orthogonal organization in the NT and superior–inferior (SI) direction; at the periphery they are mostly aligned to the limbus circumference, see Fig. 4, cf. Sánchez et al. (2014) and Simonini and Pandolfi (2015). The present version of the code uses a standard—as opposite to a patient-specific—model for the internal architecture of the collagen fiber distribution, since, at the current level of technology in ophthalmology, in vivo measurements and data are

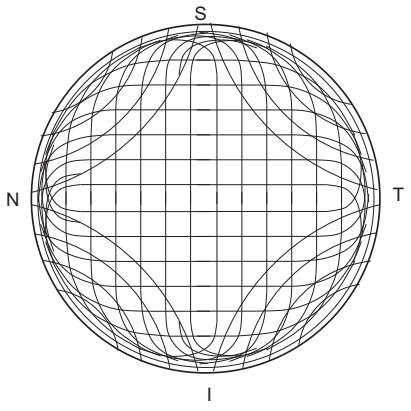

Fig. 4. Collagen fibril model. Structure of the fibril organization within the cornea, cf. Meek and Boote (2009). S denotes the superior point, I the inferior point, N the nasal point and T the temporal point.

Table 1
Material parameters used in the PSFE simulations of the puff test, cf. Simonini and Pandolfi (2015).

K (MPa)	μ_1 (MPa)	μ_2 (MPa)	k_1 (MPa)	k_2	ρ (kg/m^3)	c (s^{-1})
5.5	0.06	−0.01	0.04	200	1062	0.0 − 0.2

not available.

For the present study, we use patient-specific geometries and material constants of the five human corneas previously described in Simonini and Pandolfi (2015). We refer to the preoperative and postoperative shapes of the cornea of patients that underwent refractive surgery. In Simonini and Pandolfi (2015), the corneal models were used to estimate the variation of mechanical and refractive parameters of the cornea following the surgery. The patient-specific geometry was characterized with a set of patient-specific material properties by using an automated identification algorithm, that minimizes the geometrical differences between the preoperative and the postoperative geometry of the posterior surface of the cornea (Sánchez et al., 2014). The set of elastic material properties calibrated for the patient group in Simonini and Pandolfi (2015) has been used also in the present study, see Table 1.

2.4. Dynamic analysis

The quasi-static finite element code described in the previous section has been integrated with a module to perform dynamic analyses in a finite kinematics framework. Upon spatial discretization, the weak form of the equation of motion of an elastic system reduces to an ordinary differential equation system

$$\mathbf{M}\ddot{\mathbf{x}} + \mathbf{F}^{\text{int}} = \mathbf{F}^{\text{ext}}(t), \tag{15}$$

where $\ddot{\mathbf{x}}$ is the nodal acceleration array, $\mathbf{M}$ is the lumped and diagonal mass matrix, $\mathbf{F}^{\text{int}}$ the internal force array and $\mathbf{F}^{\text{ext}}$ the external force array. For the density ρ of the cornea we refer to the value, measured in porcine corneas, reported in Kampmeier et al. (2000), see Table 1. The external force array accounts for the IOP pressure, applied on the posterior surface of the cornea, and the air jet pressure, applied over a limited area on the anterior surface. If the system is characterized by damping, originated by internal friction or other forms of dissipation, the discretized equation of motion contains an additional term, in general assumed to be proportional to the nodal velocity array $\dot{\mathbf{x}}$,

$$\mathbf{M}\ddot{\mathbf{x}} + \mathbf{C}\dot{\mathbf{x}} + \mathbf{F}^{\text{int}} = \mathbf{F}^{\text{ext}}(t). \tag{16}$$

The damping matrix $\mathbf{C}$ can be considered as proportional to the mass matrix through a damping coefficient $c > 0$, thus $\mathbf{C} = c\mathbf{M}$. To integrate the dynamic equation in time, we resort to the classical Newmark time stepping algorithm. The method is characterized by two algorithmic parameters $0 \le \theta < 1/2$ and $0 \le \gamma \le 1$, which define the implicit or explicit nature of the formulae (Newmark, 1959); a brief outline is reported in Appendix C. For the dynamic analysis described in the following, we choose the central difference formula (θ=0 and γ=0.5). The explicit algorithm was chosen in order to exploit multiprocess computing. It is known that the central difference algorithm has order 2 accuracy, and it is conditionally stable, therefore the time step is upper-bounded by the Levi–Courant critical time step Δt_{crit}. For the adopted discretization and choice of elastic parameters, $\Delta t_{\text{crit}} = 1.27$ μs, and, in the calculations, we adopted $\Delta t = 0.51$ μs.

The simulation of the air puff test requires to execute a static analysis, to reach a status corresponding to the physiological condition of the cornea under the action of the IOP, followed by a dynamic analysis to model the action of the air puff jet. The static analysis is performed starting from the preliminarily identified stress-free geometry of the cornea, and increasing the IOP from zero to the physiological IOP. The boundary conditions imposed to the nodes at the limbus allow for the rotation of the cornea about the limbus circumference, optimizing the difference between the current model and a model that includes limbus and sclera, see Pandolfi and Holzapfel (2008) for a discussion on the choice of the boundary conditions.

During the dynamic analysis, the air jet pressure is applied over a 1.5 mm radius circular area centered at the apex of the cornea. The pressure has the functional form

$$p(t, r) = p_0 \exp\left[-64\left(\frac{t}{T} - \frac{1}{4}\right)^2\right]\exp(-0.44r^2) \tag{17}$$

where p_0 is the maximum air jet pressure, $T/2$ the duration of the air jet, and r the distance in mm from the center of the jet of a point on the corneal surface.

The choice of the spatial and temporal form of the pressure imprint deserves some comments. Since the CorVis ST system does not provide any reading of the air jet pressure, the expression (17) was chosen referring to qualitative data available from the ORA system. Note that the pressure function adopted here differs from the one used in other studies (Han et al., 2014), being symmetric and not slightly tilted in time. Our preliminary numerical experiments showed that the exact temporal and spatial form of the air jet pressure does not need to be specified accurately, as long as the air jet acts for a short time on a limited zone of the cornea. In fact, the effects of air flow transients are essentially irrelevant to the structural

response of the corneal system, although they can affect temporarily and locally the surface stresses. Moreover, alternative numerical CFD analysis of the pressure induced by the air puff jet on a fixed axis-symmetric geometry of deformed cornea (Kling et al., 2014), and the use of a complex fluid-structure interaction CFD model (Ariza-Gracia et al., 2015; Sinha Roy et al., 2015) demonstrated that the fundamental dynamics of the cornea undergoing an air puff test is not very sensitive to the specific pointwise distribution of the pressure. In fact, it has been argued that the identification of corneal biomechanical properties does not require coupled fluid–structure interaction simulations at the air–cornea interface (Sinha Roy et al., 2015).

During the dynamic analysis, the nodes at the limbus are constrained, and no displacements are allowed. This choice implies the full reflection at the limbus of the mechanical waves caused by the air jet. From the elastic material properties of the cornea (see Table 1), the shear wave speed c_s can be estimated about 7 mm/ms. During the 20 ms duration of the test, several reverberations take place across the cornea, whose in plane diameter is 11.5 mm. However, calculations show that the shear stress induced by the air jet is from one to two orders of magnitude inferior to the stress induced by the deflection, therefore there is no need to use specific expedients to avoid spurious wave interference.

Finally, we are aware that our model does not reproduce correctly the in vivo conditions of the air puff test, because it does not account explicitly for the interaction between the deformable cornea and the ocular fluid (humor aqueous) filling the anterior chamber, i. e., the spherical segment located between cornea and iris. Fluids may play a role in a dynamic test, because they interact with the posterior surface of the moving cornea, varying the local values of the IOP, and adsorbing some of the energy transmitted by the impulsive force; additionally, the shear stresses transmitted by the fluid in motion may modify the biomechanical response, slowing down the motion, with an effect that can be mistakenly attributed to the viscosity of the corneal material. Yet, this particular aspect has not been sufficiently emphasized nor modeled in the literature, although the axis-symmetric finite element model described in Kling et al. (2014) include shear stress free fluid elements.

While we are currently developing a numerical algorithm of fluid–solid interaction to analyze the problem with more accuracy, we account here for the presence of the fluid in a simplified way, by adding extra masses to the posterior nodes of the discretized cornea. We motivate our choice as follows. A structure vibrating within a fluid moves part of the surrounding fluid, producing an effect called “added mass”. In general, the added mass of thick structures (beams and plates) vibrating in air can be disregarded. By contrast, thin membranes vibrating in water are sensibly affected by the added mass, because their mass is small with respect to the mass of the mobilized water, cf. Minami (1998). In our applications, the fluid mass is computed as the total mass of the humor aqueous, and is distributed according to the variable thickness of the anterior chamber. The effect of the extra masses was to slow down the dynamic response of a few milliseconds, and to damp the oscillations observed in the final phase of the test.

The following analyses have been conducted by setting some of the parameters with values obtained from experimental data. Since in PSFE we use patient-specific geometries of the cornea, we also use the value of their physiological IOP, in average 18 mmHg=2.5 kPa. The maximum value of the pressure on the cornea in the air puff test $p_0 = 40$ kPa, cf. 25 kPa used in Ariza-Gracia et al. (2015) and 26 kPa used in Sinha Roy et al. (2015). Assuming that the 20 ms duration of the air jet equals half of the period, we set $T=40$ ms. It follows that the frequency of the air jet pulse is $\omega = 2\pi/T = 157\ \mathrm{s}^{-1}$.

The average duration of an analysis on a quad-core 64 bit Linux workstation, with 8 GB of memory and 1333 MHz, was 6 min.

3. Results

3.1. Results for the 1DOF model

According to the previous parameter estimation based on the comparison with the quasi-static results of a fully 3D finite element model, in the 1DOF model we adopted $\alpha=16$ and $\beta=0.13$. The choice of β does not account for the added mass effect. In order to compare our results with the PSFE model, we set the damping coefficient $\xi=0$ and solve Eq. (10). Results for the 1DOF model are shown in Fig. 5. In particular, Fig. 5(a) shows the mass displacement and exciting pressure time histories. The high frequency oscillations superposed to the general motion are associated to the natural frequency of the oscillator. The oscillations can be appreciated also in the velocity time history, Fig. 5(b). Fig. 5(c) shows the pressure versus the displacement diagram. As expected in dynamics, the unloading phase follows a different path with respect to the loading phase.

3.2. Results for the PSFE model

In Simonini and Pandolfi (2015) we constructed, from ocular topographer digital data, five patient-specific models of human corneas, in both preoperative and postoperative configurations. Here we use those preoperative and postoperative geometries to simulate air puff tests. One of the corneas, shown in Fig. 3, is taken as reference.

We begin by verifying the reasonability of performing purely elastic dynamic analysis with both 1DOF and PSFE models. We estimated the natural frequency of the cornea with a preliminary analysis conducted with the reference PSFE model. The analysis was extended to include a 20 ms time interval, posterior to the end of the air jet. The behavior of the cornea in this

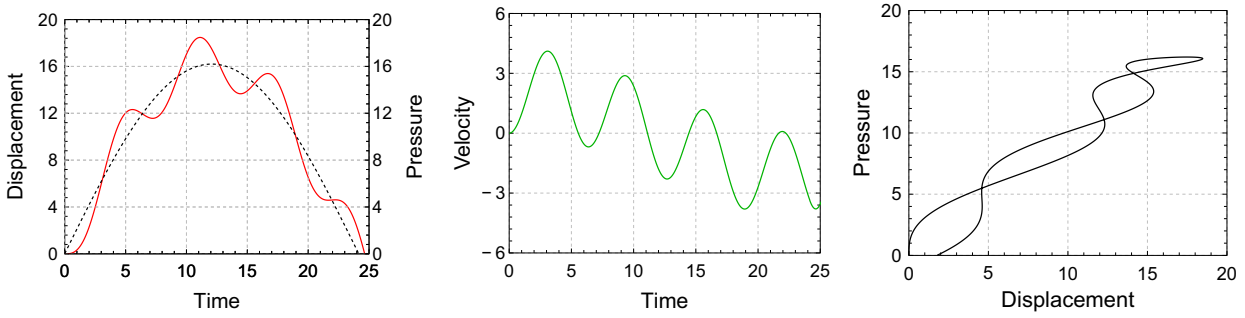

(a) Mass displacement (b) Mass velocity (c) Pressure vs mass displacement

Fig. 5. 1DOF model results. Analytical dimensionless solution for the simple model. (a) Mass displacement (solid line) and jet pressure (broken line) time history. (b) Mass velocity time history. (c) Jet pressure versus mass displacement.

time interval is characterized by a marked oscillation. We used the Fourier transform to analyze the post-test time history of the corneal apex displacement. The resulting oscillation frequency was $\Omega \approx 800$–$1200\ s^{-1}$. This value was confirmed by an additional estimation of the cornea's natural frequency based on the theory of vibrating membranes, see Appendix D. As already mentioned in the introduction, during the air puff test the filling fluids of the eye interact with the cornea in motion, and increase the "effective" corneal density several times, say 8–15. Thus the first natural frequency of the cornea–fluid system can be estimated as 25–33% of the frequency of the cornea alone, i. e., 200–400 Hz, close to the frequency of the impulse in the air puff test. This result confirms our intuition on the fundamental characteristics of the air puff test.

For the reference PSFE model, Fig. 6 reports the same information of Fig. 5, displaying the kinematics of the central point of the cornea (apex). Under pure elasticity assumptions, the PSFE results are qualitatively similar to the ones of the 1DOF model. Fig. 6(a) shows the apical displacement history and Fig. 6(b) the apical velocity history. Broken vertical lines signal the applanation times as obtained in the simulations. Fig. 6(c) plots the air jet pressure versus the displacement of the apex. The curve clearly shows the effects of dynamics in the response of the cornea to external actions, cf. also Fig. 5(c). Oscillations are related to the first natural frequency of the system, that can be also observed in Fig. 6(a).

The PSFE analyses provided several snapshots of the corneas during the test. As an example, Fig. 7 shows the views and the NT section of the reference cornea in correspondence to the maximum deflection, at about $t = 12$ ms from the beginning of the test.

Qualitative comparisons between snapshots of the numerical simulations for the reference cornea and images from CorVis ST (courtesy of Oculus Optikgerate GmbH) at characteristic times are reported in Fig. 8. In particular, Fig. 8(a) shows the configuration of the cornea at the maximum deflection, approximately at 12 ms from the beginning of the test. Fig. 8 (b) compares the snapshots of the experimental and numerical test at the time of the first applanation, approximately at 5 ms, and Fig. 8(c) does the same comparison at the time of the second applanation, approximately at 20 ms.

PSFE analyses of the air puff test have been repeated for the other four corneas, in both preoperative and postoperative configurations. These analyses provided comparable results, that have been analyzed statistically. Average dynamic parameters (time, curvature radius along the NT direction of the central concave zone, and displacement) characterizing the maximum deflection configuration of the cornea are reported in Table 2. Average dynamic parameters (time, displacement and velocity) of the cornea's apex at the first and second applanation configurations are reported in Table 3.

Fig. 9 shows the five-cornea average apex displacement versus time. The two curves refer to the preoperative and postoperative geometries, as indicated in the legend. Laser ablation reduces the central thickness of the cornea and,

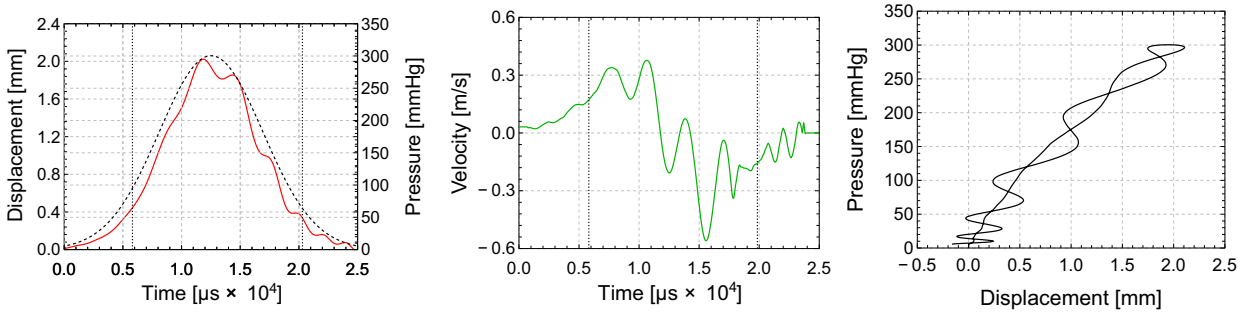

(a) Apex displacement (b) Apex velocity (c) Pressure-Apex displacement

Fig. 6. PSFE model global results. Numerical solutions for the patient-specific model. The model accounts for added mass representing the effect of humor aqueous. (a) Time history of the apex displacement (solid line) and of the air jet pressure (broken line). (b) Time history of the apex velocity. (c) Air jet pressure versus apex displacement. Broken vertical lines signal the numerical applanation times.

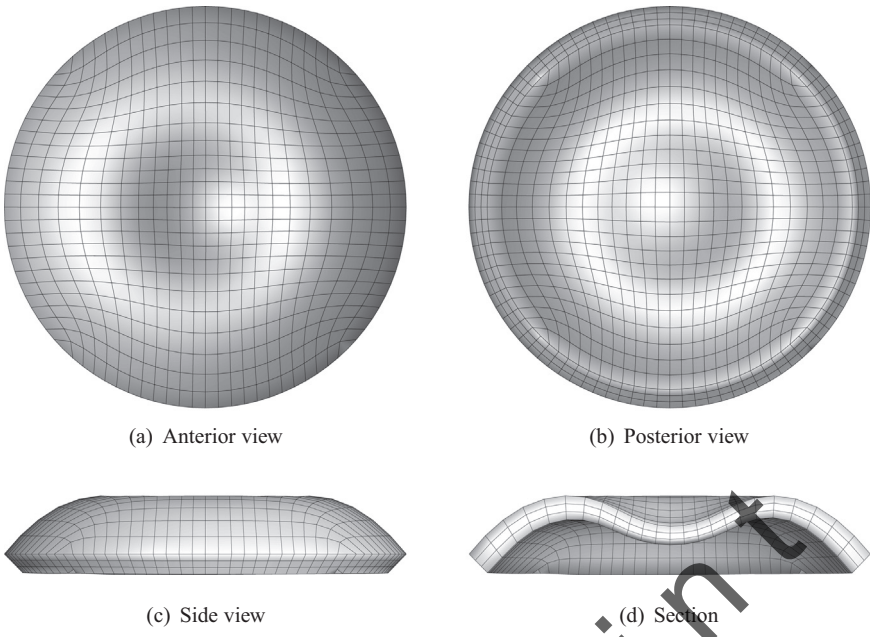

(a) Anterior view (b) Posterior view

(c) Side view (d) Section

Fig. 7. PSFE model deformed configuration. Preoperative cornea at the time of the maximum apical deflection, corresponding to $t = 12$ ms.

consequently, its stiffness. Thus postoperative corneas are more compliant and their apical displacement is larger. For the five corneas here considered, the average preoperative thickness is 543.2 ± 31.5 μm, while the average postoperative thickness is 450.1 ± 36.9 μm. At the time of the maximum deflection, the average preoperative and postoperative apical displacements for the five corneas analyzed numerically are 1.75 ± 0.27 mm and 2.02 ± 0.17 mm, respectively, with a 15.4% increment after surgery. Moreover, as it can be observed from Table 3, in postoperative corneas the first applanation time is slightly anticipated and the second applanation time delayed.

PSFE analyses provide the time history of the stress distribution. The distribution of the stress component in the NT direction for the cornea that underwent the deepest ablation is shown in Fig. 10, where preoperative and postoperative stresses are compared. Images show that the maximum deflection, characterized by a small central concavity, introduces an unusual compressive stress state in a localized region of the cornea. Accordingly, in the PSFE model the contribution of compressed collagen fibrils is excluded.

Average maximum stresses at the cornea's center, on the anterior and posterior surfaces, in both preoperative and postoperative configurations, and the percent increment in the postoperative configuration are listed in Table 4. The average increment of the anterior (posterior) surface stress is 5.3% (18%).

For the reference cornea, Fig. 11 plots the time history of air jet pressure and curvature radius associated to the NT meridian, computed from the numerical deformed geometry. The plot shows also the CH, evaluated from the numerical results according to the procedure described in Luce (2005). We note that the actual pressure space and time history used within the ORA instrument to compute the CH is not explicitly reported in Luce (2005), but it can be reasonably estimated from the information reported in the instrument documentation (Luce, 2004, 2005). In particular, accurate measurements of the time and space distribution of the pressure acting on a phantom cornea are reported in Luce (2005). Such results show

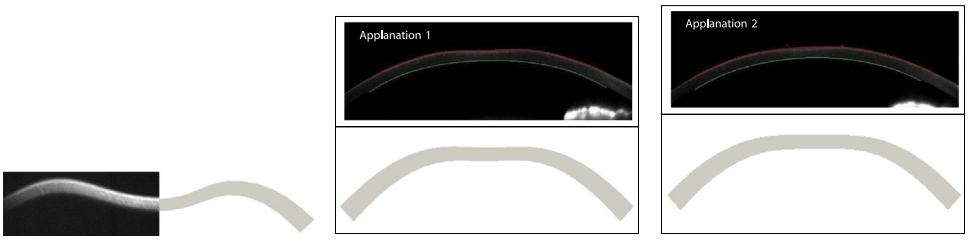

(a) Maximum deflection (b) First applanation (c) Second applanation

Fig. 8. Validation of the PSFE model. Comparison of experimental images (courtesy of Oculus Optikgerate GmbH) and snapshots of the numerical simulations of the cornea undergoing the air puff test at characteristic times. (a) Maximum deflection time; the experimental image (left) compares well with the numerical one (right). (b) First applanation, cornea going inward; both experimental (top) and numerical (bottom) shapes show a flattened central part. (c) Second applanation, cornea recovering the static configuration. both experimental (top) and numerical (bottom) shapes show a flattened central part.

Table 2
Maximum deflection of the simulated corneas. Average time, curvature radius in the NT direction, and apex displacement for all preoperative and postoperative cases.

Case	Time (μs)	NT radius (mm)	Displacement (mm)
Pre	12,609 ± 736	4.112 ± 0.305	1.75 ± 0.27
Post	12,570 ± 575	3.331 ± 0.676	2.02 ± 0.17
Diff (%)	−0.3	−19.0	15.4

that the internal plenum pressure exerted by the air jet and the actual pressure acting on the anterior surface of the cornea are characterized by the same functional form. A small delay of a few milliseconds decreasing in time, reported in Luce (2005), is assumed to be due to the transition from laminar to turbulent flow of the air jet. The delay is totally recovered at the time of the reversed configuration.

All the results here described have been obtained by assuming a perfectly elastic behavior of the material. Additional analyses have been conducted, both with the 1DOF model and the PSFE model, by introducing a small damping coefficient $c=0.2$. The effects of including damping are not appreciable in the mechanical response of the system during the action of the air jet, i.e., during the time interval in which ocular analyzer images are recorded. The influence of viscosity can be appreciated at later times, on the oscillations following the second applanation. Therefore, in the following discussion, we will refer only to the elastic response.

4. Discussion and conclusions

By using high resolution imaging, ocular analyzers (e.g., CorVis ST and ORA) monitor the deformation of a meridional section of the corneal vault induced by a high frequency air pressure impulse, with assigned duration and intensity. The air jet is applied at the center of the cornea, and causes a sudden and rapid change of configuration that is recovered by the elasticity of the stromal material. Ocular analyzer instruments have been developed for clinical applications, related to the monitoring of the IOP, the qualification of a patient for refractive surgery, and the assessment of refractive surgery outcomes. Regrettably, the current interpretation of the test data is still far from being able to provide helpful information to clinicians.

The air puff test is a dynamic test on a soft biological structure that undergoes finite deformations and large displacements. From the mechanical point of view, the dynamics of the test can be easily interpreted: under the action of the air jet the cornea deflects, leaving the stable static configuration, it reaches an unstable equilibrium configuration (the reversed concave configuration), and then it resumes the original stable shape. The process is clearly governed by several variables: the geometry of the cornea, the material properties of the cornea, the presence of fluids behind the cornea, the boundary conditions offered by the limbus, the dynamics of the air jet.

The material properties are an overall important factor in the air puff test, but unfortunately they are not known. In fact, although the human stroma has been investigated with ex vivo inflation and uniaxial tests by several researchers, the results in terms of stiffness and strength are very dispersed (Bryant and McDonnell, 1996; Hjortdal, 1996; Wollensak et al., 2003; Jayasuriya et al., 2003). Moreover, ex vivo tests damage and, in some cases, destroy the delicate structure of the tissue so that the experimental results are affected by errors that cannot be quantified easily. It follows that in vivo tests are necessary and irreplaceable to infer the stiffness and the strength of the corneal structure. Recently, air puff tests have been regarded as a possible tool for the characterization of the corneal material. The goal is not easy to be achieved, as it has been clearly stated in Ariza-Gracia et al. (2015), because the characterization of a material requires the definition of a material model, the acquisition of the exact geometry, and an identification algorithm based on advanced stress analysis procedures that can handle solid–fluid interactions.

While the present study is accurate in terms of the description of the geometry and of the structural material properties of the corneal tissue, it leaves out a number of aspects that should be considered to improve the reliability of the air puff model and make it closer to reality, i.e.: (i) modeling the fluids–structure interaction; (ii) including the effects of the surrounding tissues and of the muscles at the limbus; (iii) including the patient-specific fibril organization. Steps are moving toward this direction (Medeiros and Weinreb, 2006; Sinha Roy and Dupps, 2011; Han et al., 2014; Kling et al., 2014; Ariza-Gracia et al., 2015; Sinha Roy et al., 2015), but still many difficulties have to be overcome. Our present contribution tries to

Table 3
First and second applanation times of the simulated corneas. Average apex displacement and velocity for all preoperative and postoperative cases.

Case	App	Time (μs)	Displacement (mm)	Velocity (mm/s)
Pre	1	5878 ± 192	0.453 ± 0.016	188 ± 14
	2	19,314 ± 437	0.356 ± 0.070	−120 ± 38
Post	1	5005 ± 451	0.375 ± 0.032	186 ± 44
	2	20,558 ± 532	0.380 ± 0.102	−72 ± 60

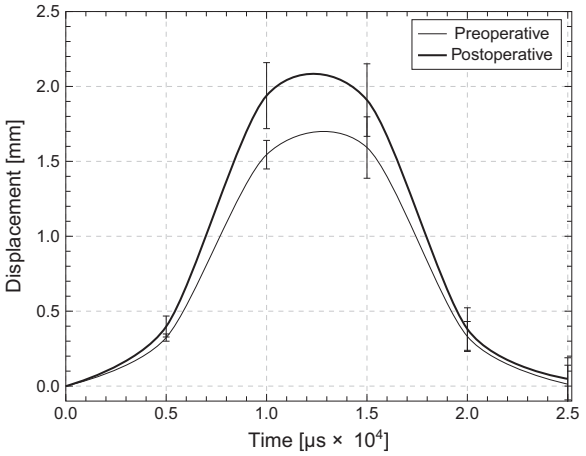

Fig. 9. Effects of corneal laser surgery. Numerical simulation results. Average (over five corneas) time history of the corneal apex displacement, in the preoperative and postoperative configurations.

elucidate the fundamental aspects of the tests, and to clarify what information can be actually derived from it.

As already mentioned, the test is characterized by a particular deformation of the cornea that deflects and passes through two local applanate configurations. The jet pressures at the applanation times are in general different, and the second is often inferior to the first. Their difference (CH) is thought to be roughly correlated to corneal stiffness and viscosity (Luce, 2005; Glass et al., 2008). The word hysteresis in mechanics is associated to dissipative phenomena, and implies irreversibility. In particular, hysteresis is often connected to viscosity or damage of the material. However, when dynamic processes are present, the mechanical response of a system is necessarily delayed with respect to the load because of the inertia. Therefore the results of the test must be analyzed within a dynamic context.

The basic features of the air puff test can be captured with a purely elastic 1DOF harmonic oscillator excited with a single half wave sinusoidal signal. Although the 1D model has been studied in Han et al. (2014), we reconsidered here a purely elastic dynamical system to rule out the relevance of viscosity. The displacement of the mass, Fig. 5(a), shows a forward motion followed by a backward motion with small oscillations. The small oscillations correspond to the natural frequency of the system. The mass velocity plot, Fig. 5(b), confirms the observation. The plot of the jet pressure versus the mass displacement, which in a static condition should be linear because of the elasticity, shows two different oscillating curves for the loading and unloading phase. This is an evident dynamic effect, related to the parameter β that measures the ratio between the excitation and natural frequencies.

A more accurate modeling of the air puff test is provided by PSFE simulations. The global response of the cornea, illustrated in Fig. 6 through the kinematics of the apex, compares qualitatively with the 1DOF analysis, cf. Fig. 5. The PSFE model shows that the first applanation is characterized by a positive velocity while the second one by a negative velocity. At the maximum deflection, the velocity is null. Furthermore, PSFE analyses provide information on the configuration of the cornea during the test. In particular, it is possible to compare the deformed shapes of the cornea with images provided by the ocular analyzers. The good correspondence between experimental and numerical images, see Fig. 8, confirms that the model is able to detect the fundamental behaviors of the system.

For both 1DOF and PSFE models, we considered a perfectly elastic behavior. Further analyses accounting for damping showed that the mechanical response of the 1DOF and PSFE models during the 40 ms of the numerical test duration is not affected by time dependency. An explanation of this is that the first natural frequency of the system (cornea and filling fluids) involved in the air puff test is of the same order of magnitude of the exciting frequency of the air puff jet. Therefore effects of inertia are dominant and the damping cannot be appreciated at early times. These observations allow giving an interpretation to the CH parameter, see Fig. 11. PSFE analyses deliver the deformed geometry of the corneas and permit to evaluate the curvature radius along any meridian at different times. When the cornea flattens, at the applanation times, the curvature radius at the apex reaches very high values. Superposing the curvature radius and the jet pressure history, we can compute the CH. The drop in pressure observed in the test between the two applanation times cannot be linked to viscous properties of the stroma, but only to its stiffness and density. As a result, data and parameters that can be derived from the analysis of the early images of ocular analyzers should be used only to characterize the elastic properties of the involved tissues. The independence of viscosity is a fundamental starting point to assess the possibility to use the air puff test for estimating the IOP, since the main features of the dynamics test are determined by the elastic properties of the cornea.

We recall that frequency of the air jet impulse is about 100 Hz, a few orders of magnitude greater than the reciprocal of any reasonable relaxation time for the material (see, e.g., the 10–100 s measured on pig corneas in Boschetti et al. (2012), 10–1000 s reported in Ahearne et al. (2007), and 5–100 s reported in Kampmeier et al. (2000)). In a recent numerical study, that reports two-dimensional finite elements simulations of the air puff test, a relaxation time of 10 ms has been derived as the result of parameter calibrations, under the assumption of linear viscoelastic behavior for the cornea (Kling et al., 2014).

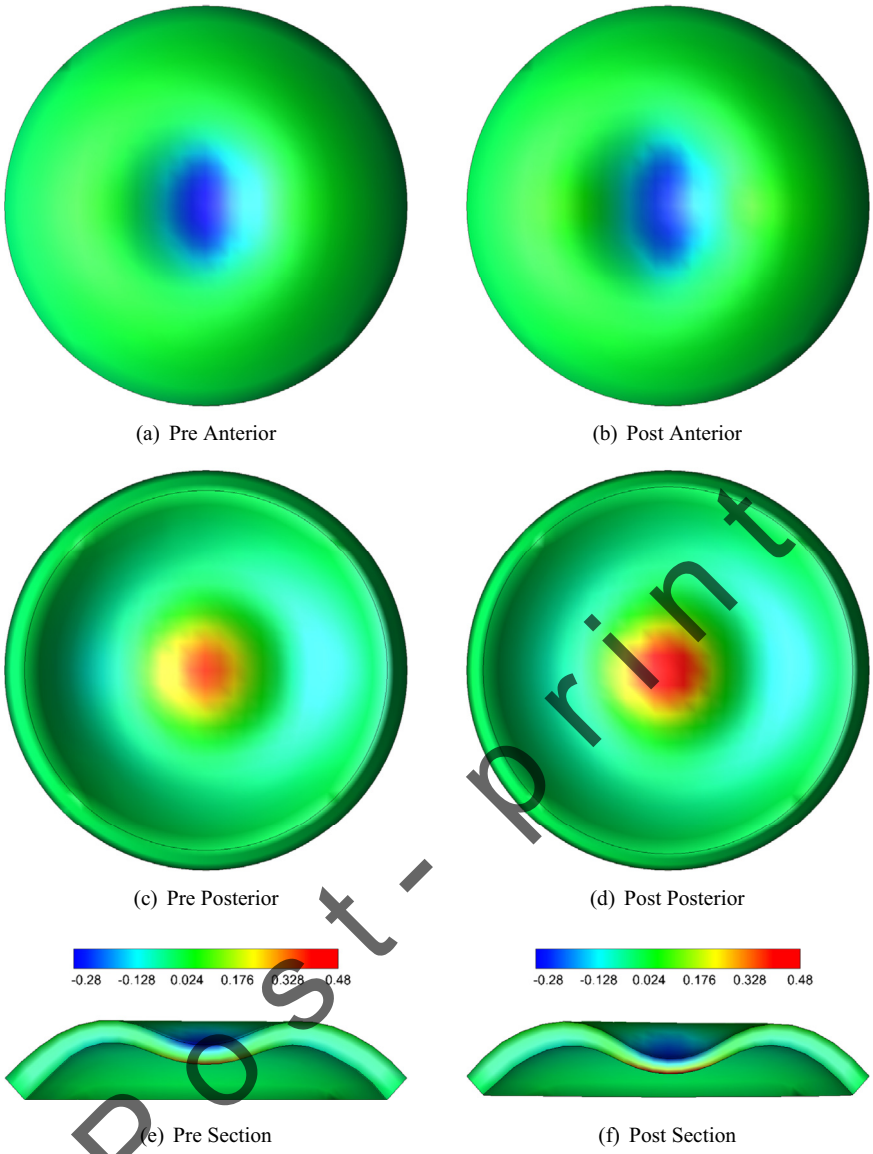

Fig. 10. Stress maps for the PSFE model. Numerical simulation results for the cornea treated with the deepest ablation. Comparison of the stress distribution at the time of maximum deflection during the air jet test between the preoperative (a–c–e) and postoperative (b–d–f) geometry. Contour levels refer to the NT component of the stress. (a and b) Anterior view. (c and d) Posterior view. (e and f) Sections.

Table 4
Cauchy stress in the NT and SI directions on the anterior (A) and posterior (P) surface of the cornea at the maximum deflection. Pre, preoperative; Post, postoperative.

Side	Case	Stress NT (kPa)	Stress SI (kPa)
A	Pre	-304.4 ± 18.7	-311.9 ± 21.1
	Post	-288.2 ± 17.5	-295.3 ± 17.9
	Diff (%)	5.3	5.3
P	Pre	395.7 ± 40.6	399.1 ± 34.6
	Post	465.8 ± 35.0	471.0 ± 38.2
	Diff (%)	17.7	18.0

This numerical value, that curiously equals half of the duration of the test, carries uncertain significance, since relaxation times for viscous materials should be determined experimentally, as the time necessary to recover a balanced stress state after a perturbation. Moreover, parameters obtained from numerical calibration have a validity inasmuch the material

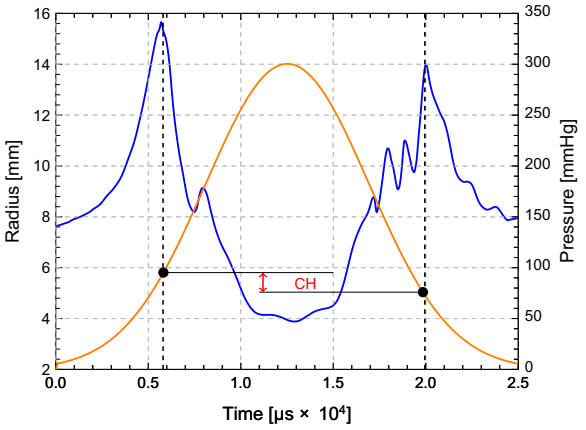

Fig. 11. Simulated calculation of CH. Numerical simulation results. Plot of the air jet pressure and of the curvature radius in the NT direction versus time.

model used in the simulations describes the actual material behavior in a realistic way. A recent study documents high frequency (100–200 MHz) ultrasonic tests on bovine corneas treated with crosslinking, a procedure used to increase the stiffness of the corneal tissue (Zhang et al., 2015). Results of ultrasonic tests are interpreted considering the cornea as a linear viscoelastic membrane modeled with a Kelvin–Voigt rheological analog. The authors report very small values for the viscous shear modulus determined experimentally, confirming the scarce relevance of viscosity in fast dynamic processes on corneas. They also observe that exciting the corneas at 100–200 Hz does not allow to distinguish the viscous behavior of untreated or treated groups. A further confirmation of our conclusion can be found in the comments to the simulations reported in Sinha Roy et al. (2015), where the authors observed a negligible phase difference between the peak air pressure and peak apical displacement. This behavior indicates that corneal viscous properties do not contribute significantly to the measured displacement of the air puff test.

Dynamic analyses provided the history of displacement, strain and stress fields during the test. Of particular interest are the stress distributions at the time of the maximum deflection of the cornea, since the configuration is very unusual for the cornea. Simulations supply the stress variation with respect to the physiological configuration and assess whether the level of stress induced by the air pressure may damage the stromal tissue. From our previous studies, we found that the Cauchy stress at the corneal apex in physiological conditions is of the order of 10–20 kPa (Sánchez et al., 2014; Simonini and Pandolfi, 2015). According to the present study, the NT and SI stress components reach their maximum at the time of the maximum deflection of the cornea. Our analyses indicate the presence a tensile stress on the posterior surface ≈ 400 kPa and a compressive stress on the anterior surface ≈ -300 kPa (see Table 4). These values compare well with results obtained by other researchers (Ariza-Gracia et al., 2015; Sinha Roy et al., 2015), considering the difference in the applied jet pressure. Dynamic stresses are 10–20 times larger than corresponding static stresses, and moreover they are in part compressive. The large increase in stress is typical of fiber reinforced biological tissues, that are characterized by a stiffening on the mechanical response with increase of the strain, both in extension and in compression. We note that, under a compressive state, collagen fibrils do not provide a mechanical support since they buckle, and the mechanical response has to rely only on the contribution of the matrix. Moreover, it is likely that the stress increase would not be a hazard for the material, since it lasts only for a few milliseconds. Dynamic stress can be therefore carried out by the elastic stiffening of the collagen fibrils, without inducing microstructural damage. However, this hypothesis needs to be verified by using microstructural multiphase models of the corneal tissue that account for the fluid flow, and are more correct to evaluate tissue damage (Cheng and Pinsky, 2013; Pinsky, 2014).

Laser corneal refractive surgery modifies, through ablation of the stromal tissue, the geometry of the anterior surface of the cornea. Geometry changes are direct, due to the tissue ablation, and indirect, due to the modified stiffness of the corneal structure. The availability of patient-specific geometries of corneas in preoperative and postoperative configurations has allowed to perform a comparative study on the effects of corneal thinning (due to refractive surgery) on the mechanical response to the air puff test.

The comparison between the preoperative and the postoperative cases in terms of apex displacement is particularly interesting. The more compliant postoperative cornea shows a larger maximum inward displacement, see Fig. 9, with a 15.4% increment with respect to the preoperative case, see also Table 2. From the same table it is possible to notice that the average NT curvature radius is smaller for postoperative corneas, with a 19% decrement with respect to the preoperative case.

As far as the stress distribution is concerned, in physiological (static) conditions postoperative corneas experience higher stresses, in the average 25% larger than preoperative corneas (Sánchez et al., 2014; Simonini and Pandolfi, 2015). During the dynamic test, with respect the normal corneas, the thinned corneas tend to behave more like membranes than like shells. The numerical results show that, in the concave configurations, the anterior and posterior stresses are both higher (the anterior stress being negative is smaller in absolute value), which implies an increment of the average membrane stress, see

Table 4. The analysis of the maximum stresses in individual corneas confirms that thinner corneas experience higher stresses during the air puff test. In the average, the higher compliance and the smaller mass of the postoperative corneas cause the anticipation of the first applanation time up to 14.8% and the retardation of the second applanation time up to 5.9%.

It has been recently proposed (Kling and Marcos, 2013) that ocular muscles may be involved in the air puff process, resulting in a rigid movement of the cornea in the thickness direction and in some damping effects, visible from the long-tail in the deformation-time curve reported by CorVis ST (see the first inset figure of Fig. 1). The current study does not consider the presence of ocular muscles, mainly because we believe that the presence of fluids interacting with the posterior surface of the cornea is the main motivation of such long tail.

Taking a different approach with respect to other recent contributions, that use simplified material models and conduct parametric analyses on a few material parameters (Kling and Marcos, 2013; Kling et al., 2014; Han et al., 2014), in the present study we use a patient-specific cornea geometry and previously identified patient-specific elastic material properties. The cornea model is reasonably accurate, in particular it accounts for anisotropy that is neglected in other models. It has been used to prove that the main features of the air puff test are dominated by elasticity, and we believe that the puff-test, suitably supported by geometrical patient-specific models, can be used to characterize the elastic properties of the cornea. Our understanding is that patent-specific material and structural properties cannot be estimated through the air puff test, unless the test conditions can be varied several times on the same eye. In a companion work, we conducted parametric analyses on the influence of the known actions (air puff intensity and IOP) on the outcomes of the tests (Simonini and Pandolfi, 2015).

In conclusion, the most important contribution of this study must be sought in the correctness, within the limitations that we have clearly stated, of both analytical and numerical approaches, where we avoided simplifying assumptions or the introduction of unavailable mechanical parameters of adjacent tissues. A second aim was to rule out the importance of viscosity in the main aspects of the test, e.g., the first and second applanations, and therefore to exclude that any fast contactless test can provide information on viscous properties of the cornea. Finally, we demonstrated that some of the parameters provided by air puff instruments (i.e., CH) are meaningless.

We remark that the added mass approach is suitable only to model the first part of the process, from the application of the air puff to the second applanation. To capture the overall damped response following the second applanation, due to the recoil effect exerted by the fluid in motion it would be necessary to model the fluid–structure interaction. To date, we have extended the present study to a more complete model of the anterior chamber of the eye, that includes fluid–solid interaction to account for the presence of the filling fluids behind the cornea. Once the fluid–structure interaction process taking place during the air puff test would have been clarified and correctly modeled, it would be possible to account realistically for the presence of ocular muscles.

Acknowledgments

We are grateful to Paolo Biscari (Physics Department, Politecnico di Milano) for helpful discussions.

Appendix A

Briefly, a target finite element mesh $\mathcal{M}_0$ is reconstructed from digital clinical data. The target nodal coordinates $\mathbf{x}$ correspond to the sum of the unknown stress-free coordinates $\mathbf{X}$ and of the nodal displacements $\mathbf{u}$ caused by the application of the IOP

$$\mathbf{x} = \mathbf{X} + \mathbf{u}. \tag{A.1}$$

An iterative procedure performs static analyses at the physiological IOP pressure and evaluates the nodal displacements. At the first iteration, the algorithm assumes $\mathbf{X}=\mathbf{x}$. The computed displacements are subtracted to the target nodal coordinates to provide an estimate of the stress-free coordinates $\mathbf{X}$. Thus, a new analysis is performed. The procedure is interrupted when a suitable norm of the difference between the stress-free coordinates evaluated in two successive iterations reduces below a given tolerance, specifically $\varepsilon = 10^{-6}$.

Appendix B

The first and the second invariant of the isochoric Cauchy–Green deformation tensor are defined as

$$\overline{I}_1 = \operatorname{tr} \overline{\mathbf{C}}, \quad \overline{I}_2 = \tfrac{1}{2}[(\operatorname{tr} \overline{\mathbf{C}})^2 - \operatorname{tr}(\overline{\mathbf{C}}^2)]. \tag{B.1}$$

The two pseudo-invariants $\overline{I}_{4_M}$, $M = 1, 2$ are defined as

$$\overline{I}^{*}_{4M} = \mathbf{H}_M : \overline{\mathbf{C}}. \tag{B.2}$$

The structure tensor $\mathbf{H}_M$ is defined as

$$\mathbf{H}_M = \kappa_M \mathbf{I} + (1 - 3\kappa_M)\mathbf{A}_M, \quad \mathbf{A}_M = \mathbf{a}_M \otimes \mathbf{a}_M, \tag{B.3}$$

$\mathbf{I}$ being the identity tensor. The scalar parameter κ_M depends of the chosen spatial distribution of the fibrils orientation $b_M(\mathbf{x})$. The two terms

$$K^{*}_{M} = k_{2M} + 2\, k^{2}_{2M}\left(\overline{I}^{*}_{4M} - 1\right)^{2} \tag{B.4}$$

and

$$\sigma^{2}_{I_4 M} = \overline{\mathbf{C}} : \langle \mathbf{A}_M \otimes \mathbf{A}_M \rangle : \overline{\mathbf{C}} - \left(\mathbf{H}_M : \overline{\mathbf{C}}\right)^{2}. \tag{B.5}$$

are introduced to include the variance of the fibril orientation distribution in the material model, see Pandolfi and Vasta (2012).

Appendix C

Given the time interval $[0 - T_F]$ of the process, we wish to obtain the configuration of the system at discrete times t_n, with $t_0 = 0$, t_1, …, t_n, …$t_N = T_F$. The initial conditions are assigned in terms of initial positions $\mathbf{x}(0) = \mathbf{x}_0$ and velocities $\dot{\mathbf{x}}(0) = \dot{\mathbf{x}}_0$. By assuming the solution to be known at the time step t_n, the solution at time t_{n+1} is given by the formulae

$$\mathbf{x}_{n+1} = \mathbf{x}_n + \Delta t \dot{\mathbf{x}}_n + \frac{\Delta t_n^2}{2}\left[(1 - 2\theta)\ddot{\mathbf{x}}_n + 2\theta \ddot{\mathbf{x}}_{n+1} \right], \tag{C.1}$$

$$\dot{\mathbf{x}}_{n+1} = \dot{\mathbf{x}}_n + \Delta t\,[(1 - \gamma)\ddot{\mathbf{x}}_n + \gamma \ddot{\mathbf{x}}_{n+1}], \tag{C.2}$$

where $\Delta t = t_{n+1} - t_n$. In the calculations we follow a predictor/corrector strategy. In the predictor stage, the updated positions and velocities are characterized by the known quantities at the end of the previous step

$$\mathbf{x}^{\mathrm{pre}}_{n+1} = \mathbf{x}_n + \Delta t \dot{\mathbf{x}}_n + \frac{\Delta t^2}{2}(1 - 2\theta)\ddot{\mathbf{x}}_n, \tag{C.3}$$

$$\dot{\mathbf{x}}^{\mathrm{pre}}_{n+1} = \dot{\mathbf{x}}_n + \Delta t (1 - \gamma)\ddot{\mathbf{x}}_n. \tag{C.4}$$

Predictors are used for the evaluation of the internal force array, by means of the standard finite element integration and assembling

$$\mathbf{F}^{\mathrm{int}}_{n+1} = \mathbf{F}^{\mathrm{int}}\left(\mathbf{x}^{\mathrm{pre}}_{n+1}, \dot{\mathbf{x}}^{\mathrm{pre}}_{n+1}\right), \tag{C.5}$$

and for the calculation of the accelerations, from Eq. (16), as

$$\ddot{\mathbf{x}}_{n+1} = \mathbf{M}^{-1}\left[\mathbf{F}^{\mathrm{ext}}(t_{n+1}) - \mathbf{F}^{\mathrm{int}}_{n+1} \right] - c\, \dot{\mathbf{x}}^{\mathrm{pre}}_{n+1}. \tag{C.6}$$

The corrector stage provides the updated positions and velocities as

$$\mathbf{x}_{n+1} = \mathbf{x}^{\mathrm{pre}}_{n+1} + \theta\, \Delta t_n^2\, \ddot{\mathbf{x}}_{n+1}, \tag{C.7}$$

$$\dot{\mathbf{x}}_{n+1} = \dot{\mathbf{x}}^{\mathrm{pre}}_{n+1} + \gamma\, \Delta t\, \ddot{\mathbf{x}}_{n+1}. \tag{C.8}$$

Appendix D

The natural frequencies of the cornea can be roughly estimated by referring to a shallow membrane model, by neglecting the bending effects. The shallowness of a membrane is measured by the ratio between the rise and the diameter of the cup; in the case of the cornea the shallowness is ≈ 0.2. The first two natural frequencies corresponding to symmetric modes of a shallow membrane are the so-called $\omega_{(0,1)}$, $\omega_{(0,2)}$ frequencies. The two numbers α and β in the index $_{(\alpha,\beta)}$ indicate the number of line nodes in the meridional and circumferential direction, respectively. The two natural frequencies are computed as

$$\omega_{(0,1)} = 2.4\frac{c_L}{D_c}, \quad \omega_{(0,2)} = 5.52\frac{c_L}{D_c}, \quad c_L = \sqrt{\frac{\sigma}{\rho_c}}, \tag{D.1}$$

where c_L is the longitudinal wave speed in the membrane, i.e., the square root of the ratio between the membrane stress σ

and the density ρ_c, and D_c is the diameter of the shallow cup. By assuming $\sigma = 15$ kPa (i. e., the average stress in the static conditions), $\rho_c = 1062\ \mathrm{kg/m^3}$, and using the corneal diameter of the reference patient is $D_c = 11.5$ mm, we obtain $\omega_{(0,1)} \approx 808\ \mathrm{s^{-1}}$ and $\omega_{(0,2)} \approx 1859\ \mathrm{s^{-1}}$. These values are in a good agreement with the frequencies evaluated with the Fourier transform and justify the choice of the value for the parameter β in the 1DOF calculations.

References

Ahearne, M., Yang, Y., Then, K.Y., Liu, K.-K., 2007. An indentation technique to characterize the mechanical and viscoelastic properties of human and porcine corneas. Ann. Biomed. Eng. 35 (9), 1608–1616.

Alastrué, V., Calvo, B., Peña, E., Doblaré, M., 2006. Biomechanical modeling of refractive corneal surgery. J. Biomech. Eng. 128, 150–160.

Ambrósio, R.J., Nogueira, L.P., Caldas, D.L., Fontes, B.M., Luz, A., Cazal, J.O., Alves, M.R., Belin, M.W., 2011. Evaluation of corneal shape and biomechanics before lasik. Int. Ophthalmol. Clin. 51 (2), 11–38.

Ariza-Gracia, M.A., Zurita, J.F., Piñero, J.F., ad Rodriques-Matas, D.P., Calvo, B., 2015. Coupled biomechanical response of the cornea assessed by non-contact tonometry. A simulation study. PLoS ONE 10 (3), e0121486.

Boschetti, F., Triacca, V., Spinelli, L., Pandolfi, A., 2012. Mechanical characterization of porcine corneas. J. Biomech. Eng. 134 (3), 031003.

Bryant, M.R., McDonnell, P.J., 1996. Constitutive laws for biomechanical modeling of refractive surgery. J. Biomech. Eng. 118 (4), 473–481.

Cabrera Fernández, D., Niazi, A.M., Kurtz, R.M., Djotyan, J.P., Juhasz, T., 2005. Finite element analysis applied to cornea reshaping. J. Biomed. Opt. 10 (6), 064018.

Cheng, X., Pinsky, P.M., 2013. Mechanisms of self-organization for the collagen fibril lattice in the human cornea. J. R. Soc. Interface 10 (87).

Chihara, E., 2008. Assessment of true intraocular pressure: the gap between theory and practical data. Surv. Ophthalmol. 53 (3), 203–218.

Elsheikh, A., 2010. Finite element modeling of corneal biomechanical behavior. J. Refract. Surg. 26 (4), 289–300.

Farandos, N.M., Yetisen, A.K., Monteiro, M.J., Lowe, C.R., Yun, S.H., 2015. Contact lens sensors in ocular diagnostics. Adv. Healthcare Mater. 4 (6), 792–810.

Gasser, T.C., Ogden, R.W., Holzapfel, G.A., 2006. Hyperelastic modelling of arterial layers with distributed collagen fibre orientations. J. R. Soc. Interface 3, 15–35.

Glass, D.H., Roberts, C.J., Litsky, A.S., Weber, P.A., 2008. A viscoelastic biomechanical model of the cornea describing the effect of viscosity and elasticity on hysteresis. Invest. Ophthalmol. Vis. Sci. 49 (9), 3919–3926.

Goldmann, H., Schmidt, T.H., 1957. Uber applanations-tonometrie. Ophtalmologica 134, 221–242.

Han, Z., Tao, C., Zhou, D., Sun, Y., Zhou, C., Ren, Q., Roberts, C.J., 2014. Air puff induced corneal vibrations: theoretical simulations and clinical observations. J. Refract. Surg. 30 (3), 208–213.

Hjortdal, J.O., 1996. Regional elastic performance of the human cornea. J. Biomech. 29, 931–942.

Hon, Y., Lam, A.K.C., 2013. Corneal deformation measurement using Scheimpflug noncontact tonometry. Optomet. Vis. Sci. 90 (1), e1–e8.

Hong, J., Xu, J., Wei, A., Deng, S.X., Cui, X., Yu, X., Sun, X., 2013. A new tonometer—the Corvis ST tonometer: clinical comparison with noncontact and Goldmann applanation tonometers. Invest. Ophthalmol. Vis. Sci. 54 (1), 659–665.

Jayasuriya, A.C., Ghosh, S., Scheinbeim, J.I., Lubkin, V., Bennett, G., Kramer, P., 2003. A study of piezoelectric and mechanical anisotropies of the human cornea. Biosens. Bioelectron. 18, 381–387.

Kampmeier, J., Radt, B., Birngruber, R., Brinkmann, R., 2000. Thermal and biomechanical parameters of porcine cornea. Cornea 19 (3), 355–363.

Kling, S., Marcos, S., 2013. Contributing factors to corneal deformation in air puff measurements. Invest. Ophthalmol. Vis. Sci. 54, 5078–5085.

Kling, S., Bekesi, N., Dorronsoro, C., Pascual, D., Marcos, S., 2014. Corneal viscoelastic properties from finite-element analysis of in vivo air-puff deformation. PLoS ONE 9 (8), e104904.

Luce, D.A., 2004. Tonometer Calibration Tool, 01.

Luce, D.A., 2005. Determining in vivo biomechanical properties of the cornea with an ocular response analyzer. J. Cataract Refract. Surg. 31 (1), 156–162.

Martinez de la Casa, J.M., Garcia-Feijoo, J., Fernandez-Vidal, A., Mendez-Hernandez, C., Garcia-Sanchez, J., 2006. Ocular response analyzer versus Goldmann applanation tonometry for intraocular pressure measurements. Invest. Ophthalmol. Vis. Sci. 47 (10), 4410–4414.

Medeiros, F.A., Weinreb, R.N., 2006. Evaluation of the influence of corneal biomechanical properties on intraocular pressure measurements using the ocular response analyzer. J. Glaucoma 15 (5), 364–370.

Meek, K.M., Boote, C., 2009. The use of X-ray scattering techniques to quantify the orientation and distribution of collagen in the corneal stroma. Prog. Retinal Eye Res. 28 (5), 369–392.

Minami, H., 1998. Added mass of a membrane vibrating at finite amplitude, 12, 912–932.

Newmark, N.M., 1959. A method of computation for structural dynamics. In: Proceedings of ASCE, vol. 85, pp. 67–94.

Pandolfi, A., Holzapfel, G.A., 2008. Three-dimensional modelling and computational analysis of the human cornea considering distributed collagen fiber orientation. J. Biomech. Eng. 130, 061006.

Pandolfi, A., Manganiello, F., 2006. A material model for the human cornea. Biomech. Model. Mechanobiol. 5, 237–246.

Pandolfi, A., Vasta, M., 2012. Fiber distributed hyperelastic modeling of biological tissues. Mech. Mater. 44, 151–162.

Pandolfi, A., Fotia, G., Manganiello, F., 2009. Finite element simulations of laser refractive corneal surgery. Eng. Comput. 25 (1), 15–24.

Piñero, D.P., Alcón, N., 2014. In vivo characterization of corneal biomechanics. J. Cataract Refract. Surg. 40 (6), 870–887.

Pinsky, P.M., van der Heide, D., Chernyak, D., 2005. Computational modeling of mechanical anisotropy in the cornea and sclera. J. Cataract Refract. Surg. 31 (1), 136–145.

Pinsky, P.M., 2014. Three-dimensional modeling of metabolic species transport in the cornea with a hydrogel intrastromal inlay. Invest. Ophthalmol. Vis. Sci. 55, 3093–3106.

Roberts, C., 2014. Concepts and misconceptions in corneal biomechanics. J. Cataract Refract. Surg. 40 (6), 862–869.

Sánchez, P., Moutsouris, K., Pandolfi, A., 2014. Biomechanical and optical behavior of human corneas before and after photorefractive keratectomy. J. Cataract Refract. Surg. 40 (6), 905–917.

Simonini, I., Pandolfi, A., 2015. Customized finite element modelling of the human cornea. PLoS ONE 10 (6), e0130426.

Simonini, I., Pandolfi, A., 2015. The influence of intraocular pressure and air jet pressure on corneal contactless tonometry tests. J. Mech. Behav. Med. Biomater., Online First (July), pp. 1–15.

Sinha Roy, A., Dupps Jr., W.J., 2011. Patient-specific modeling of corneal refractive surgery outcomes and inverse estimation of elastic property changes. J. Biomech. Eng. 133 (1), 011002.

Sinha Roy, A., Kurian, M., Matalia, H., Shetty, R., 2015. Air-puff associated quantification of non-linear biomechanical properties of the human cornea in vivo. J. Mech. Behav. Med. Biomater. 48 (1), 173–182.

Wollensak, G., Spoerl, E., Seiler, T., 2003. Stress-strain measurements of human and porcine corneas after riboflavin-ultraviolet-a-induced cross-linking. J. Cataract Refract. Surg. 29, 1780–1785.

Zhang, X., Yin, Y., Guo, Y., Fan, N., Lin, H., Liu, F., Diao, X., Dong, C., Chen, X., Wang, T., Chen, S., 2015. Measurements of quantitative viscoelasticity in bovine corneas based on lamb wave dispersion properties. Ultrasounds Med. Biol. 41 (5), 1461–1472.